Nano-Micro Letters
e-ISSN 2150-5551
CN 31-2103/TB
ARTICLE
https://doi.org/10.1007/s40820-025-01954-3

Cite as
Nano-Micro Lett.
(2026) 18:107

Received: 23 June 2025
Accepted: 16 September 2025

Exposing Zn(002) Texture with Sucralose Additive for Stable and Dendrite-Free Aqueous Zinc-Ion Batteries

Feiyu Tao[1,4], Yingke Ren[2], Li'e Mo[3], Yifan Wang[3], Yang Huang[3], Hong Zhang[5], Chengwu Shi[1], Zhaoqian Li[1,3] ✉, Jiaqin Liu[1,6], Lei Chen[4] ✉, Linhua Hu[3] ✉, Yucheng Wu[1] ✉

HIGHLIGHTS

- Sucralose (SCL) has been unveiled as an electrolyte additive to promote the exposure of the Zn(002) texture.
- SCL has been verified to disrupt the solvation structure around zinc ions and reduce water activity on Zn anode.
- After adding SCL additives, Zn//Zn battery achieves the cycling lifespan of 171 h at 30 mA cm^{-2}–30 mAh cm^{-2} (DOD = 73.3%). Zn//Cu battery achieves a high Coulombic efficiency of 99.61% at 0.2 mA cm^{-2} with 0.2 mAh cm^{-2}.

ABSTRACT Aqueous zinc-ion batteries (AZIBs) are currently confronted with the challenge of achieving long-term cyclic stability under high current densities. This issue is primarily attributed to the excessive growth of dendrites and the occurrence of significant side reactions. Herein, sucralose (SCL), as an electrolyte additive, has been used to promote the exposure of the Zn(002) texture. The introduction of SCL can adjust the Zn^{2+} nucleation and diffusion along different crystal facets, promoting the exposure of the Zn(002) texture. By substituting water molecules in the $[Zn(H_2O)_6]^{2+}$, SCL reconfigures the hydrogen bond network in the electrolyte, reconstructing the solvation structure and suppressing the hydrogen evolution reaction. Consequently, the Zn//Zn symmetric battery exhibits long-term cycling stability of over 4900 h at 1 mA cm^{-2}–1 mAh cm^{-2}. Even at a harsh condition of 30 mA cm^{-2}–30 mAh cm^{-2} (DOD = 73.3%), it can stably cycle for 171 h. The CE of the Zn//Cu half battery reaches 99.61% at 0.2 mA cm^{-2} with 0.2 mAh cm^{-2}. Employing the optimized electrolyte, after 500 cycles, a high specific capacity of 420 mAh g^{-1} can be retained for the $NH_4V_4O_{10}$//Zn full battery at 500 mA g^{-1}, corresponding to a capacity retention of 90.7%.

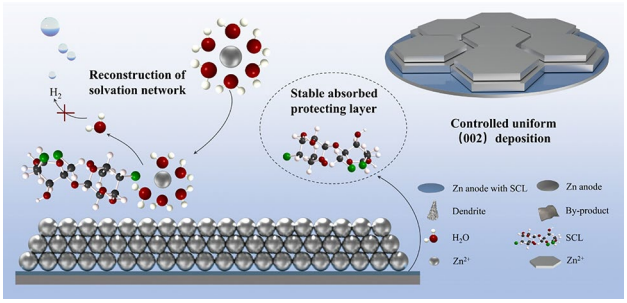

KEYWORDS Aqueous zinc-ion batteries; Zinc anode; Oriented growth; (002) texture

✉ Zhaoqian Li, zqli@hfit.edu.cn; Lei Chen, chenlei@just.edu.cn; Linhua Hu, lhhu@rntek.cas.cn; Yucheng Wu, ycwu@hfut.edu.cn
[1] School of New Energy Engineering, Hefei Institute of Technology, Anhui 238076 Hefei, People's Republic of China
[2] College of Science, Hebei University of Science and Technology, Hebei 050018 Shijiazhuang, People's Republic of China
[3] Key Laboratory of Photovoltaic and Energy Conservation Materials, CAS, Institute of Solid State Physics, Hefei Institutes of Physical Science, Chinese Academy of Sciences, Anhui 230031 Hefei, People's Republic of China
[4] School of Environmental and Chemical Engineering, Jiangsu University of Science and Technology, 212003 Zhenjiang, People's Republic of China
[5] Hebei Computational Optical Imaging and Photoelectric Detection Technology Innovation Center, Hebei International Joint Research Center for Computational Optical Imaging and Intelligent Sensing, School of Mathematics and Physics Science and Engineering, Hebei University of Engineering, Hebei 056038 Handan, People's Republic of China
[6] School of Chemistry, Beijing University of Chemical Technology, 100029 Beijing, People's Republic of China

Published online: 09 January 2026
Shanghai Jiao Tong University Press
Springer

1 Introduction

Aqueous zinc-ion batteries (AZIBs) are increasingly recognized as attractive candidates for energy storage applications, owing to their inherent safety, cost-effectiveness, and eco-friendly characteristics [1–4]. Zinc, as an anode material, offers exceptional theoretical specific capacity (820 mAh g^{-1}) and volumetric capacity (5855 mAh cm^{-3}) [5–7], making it an attractive candidate for grid-scale energy storage applications. Nevertheless, commercial Zn foil cannot work stably under high depth of discharge (DOD) and current density, impeding the widespread commercialization of ZIBs [8]. High DOD leads to an uneven distribution of local Zn^{2+} concentration at the electrode surface, causing 3D Zn deposition with arbitrary orientation, which results in severe dendrites [9–12]. Uneven zinc stripping during the discharge process also exacerbates the formation of holes and further promotes dendrite growth, significantly compromising the integrity and stability of the Zn anode [13]. Under high current densities, except for the generated hydrogen gas, the enhanced hydrogen evolution reaction may affect the local pH environment near the electrode surface, resulting in the generation of detrimental side products that can adversely influence zinc deposition.

Alleviating zinc dendrite growth is primary to improve the stability of ZIBs [14, 15]. Zn, as a hexagonal close-packed metal, exhibits the primary crystal facets of (002), (100), and (101) planes [16]. During deposition, the Zn(101) and (100) facets with larger angles to the substrate often result in uneven zinc deposition. In contrast, if Zn^{2+} is deposited along the Zn(002) crystal plane, the Zn(002) tends to deposit on the substrate in a parallel type, a planar and smooth zinc deposition layer can be achieved [17]. Additionally, the Zn(002) plane, with the lowest surface energy [18], has lower electrochemical activity toward hydrogen evolution reaction (HER) and corrosion reactions [19]. Controlling the preferential crystal orientation is crucial for AZIBs, particularly in suppressing dendrite growth and improving battery stability [20, 21].

Herein, a sweetener, sucralose (SCL), was introduced into the $Zn(OTF)_2$ electrolyte to enhance the reversibility of the zinc anode. Due to the strong interaction, the SCL firmly adsorbs on the Zn surface. The as-formed dynamic protection layer can effectively repel active water molecules at the interface, inhibiting water-induced side reactions and expanding the electrochemical window of the electrolyte. After binding with the SCL molecules, the suppressed zinc deposition along the (002) direction leads to a large areal exposure of the (002) facet, which facilitates highly reversible and dendrite-free Zn anodes. Benefiting from the introduction of SCL, the Zn//Zn symmetric battery exhibits prolonged lifespan of 4900 h at 1 mA cm^{-2}–1 mAh cm^{-2} and 171 h at 30 mA cm^{-2}–30 mAh cm^{-2} (DOD = 73.3%). The CE of the Zn//Cu half battery reaches 99.61% at 0.2 mA cm^{-2} with 0.2 mAh cm^{-2}, confirming the high plating/stripping reversibility of the zinc anode. The $NH_4V_4O_{10}$//Zn full battery, after being cycled 500 times at 500 mA g^{-1}, keeps a specific capacity of 420 mAh g^{-1} (a capacity retention of 90.7%). This work highlights the preferential Zn deposition facilitated by the SCL electrolyte additive for achieving highly reversible AZIBs.

2 Experimental Section

2.1 Electrolytes and Cathode Material Preparation

All reagents were used without further purification. The $Zn(OTF)_2$ electrolyte was prepared by dissolving 0.1 mol of $Zn(CF_3SO_3)_2$ (Sigma-Aldrich) in 100 mL of deionized water. The SCL/$Zn(OTF)_2$ electrolyte was subsequently formulated by adding 4, 5, and 6 wt% of sucralose to the as-prepared $Zn(CF_3SO_3)_2$ solution. The cathode material was synthesized via a hydrothermal process. In detail, 7.5 mmol of $H_2C_2O_4{\cdot}2H_2O$ (Sinopharm, 99.8%) was dissolved in deionized water at 60 °C. Subsequently, under constant stirring, 10 mmol of NH_4VO_3 (Adamasbeta) was incorporated into the solution. The ensuing uniform mixture was then transferred into a 100 mL Teflon-lined autoclave and subjected to heating in a temperature-regulated oven at 180 °C for 24 h. Subsequently, the resulting product was meticulously rinsed with deionized water via centrifugation and then dried at 80 °C.

2.2 Materials Characterization

XRD patterns were collected using a Rigaku Smart Lab 9KW X-ray diffractometer from Japan, operating with Cu-Kα radiation of wavelength 1.540593 nm. FESEM (SU8020) at 10 kV acceleration voltage was used to study the samples' surface features. XPS analysis was done on a

https://doi.org/10.1007/s40820-025-01954-3

Kratos AXIS Supra + spectrometer, with energies relative to binding calibrated by the C 1 *s* peak at 284.8 eV, with the aim of taking into account charging effects on the surface. Surface topography of the zinc electrodes was evaluated using a three-dimensional digital microscope (VK-X250). In situ optical microscopy observations were carried out with a custom-designed open electrochemical cell. The pH values were determined with a Mettler Toledo pH meter. Zeta potential measurements were carried out using a Zeta Sizer NANOPLUS instrument. For zeta potential testing, liquid samples were prepared by ultrasonically dispersing the Zn deposits (obtained at 5 mA cm^{-2} with a capacity of 5 mAh cm^{-2}) from Cu foil into 10 mL of electrolyte to form uniform suspensions. All NMR spectra were acquired on a Bruker AVANCE 600 MHz spectrometer (Germany). Raman spectra were obtained using a WITec alpha300R spectrometer equipped with a 532 nm diode-pumped solid-state laser, covering a spectral range from 4000 to 100 cm^{-1}.

2.3 Electrochemical Characterization

Potentiostatic current–time transient measurements were conducted under a constant overpotential of -150 mV. LSV was performed on a CHI660E electrochemical workstation. Stainless steel was used as the working electrode, and a zinc plate functioned as both the counter and reference electrodes. The electrolyte's nucleation overpotential was ascertained through cyclic voltammetry at a scan rate of 1 mV s^{-1}. The differential capacitance was determined using the equation: $C = -(\omega Z_m)^{-1}$. A frequency of 1 Hz was used for this calculation. Tafel polarization curves were acquired by sweeping the potential from -0.5 to 0.5 V at a rate of 5 mV s^{-1} in Zn//Zn symmetric cells. In these symmetric batteries, the zinc foil thickness was 100 µm when tested at 1 mA cm^{-2}, while a reduced thickness of 70 µm was used for tests at 30 mA cm^{-2}. For Zn//Cu and full batteries, the zinc foil thickness remained at 100 µm. The cathode material used in the full batteries was $NH_4V_4O_{10}$. Long-term cycling performance and Coulombic efficiency (CE) were evaluated using a battery test system (BTS 3000, Neware, Shenzhen, China). Activation energy (E_a) was derived from electrochemical impedance spectroscopy (EIS) measurements conducted at varying temperatures. This analysis was based on the Arrhenius equation:

$$R_{ct}^{-1} = A\, e^{-\frac{E_a}{RT}} \quad (1)$$

2.4 Density Functional Theory Method

Density functional theory (DFT) calculations were performed using the *Vienna* Ab initio Simulation Package (VASP). The exchange–correlation energy was evaluated using the GGA method with the PBE functional. A plane-wave basis set at a 450 eV kinetic energy cutoff was applied in all computations. During structural optimization, ionic forces were relaxed to below 0.02 eV $Å^{-1}$, and the electronic convergence criterion was set at 10^{-5} eV. A five-layer Zn surface supercell containing 64 atoms per layer was used to model the Zn facet. The adsorption energy between the Zn surface and various molecules was calculated using the following expression:

$$\Delta E_{ad} = E_{Zn-slab+molecules} - E_{Zn-slab} - E_{molecules} \quad (2)$$

The climbing image nudged elastic band (CI-NEB) method, implemented via the VTST Tools within the VASP framework, was employed to determine the migration energy barrier. The migration energy is defined as the relative energy between adjacent high-symmetric zinc adsorption positions along the migration path.

Molecular dynamics simulations were executed via the Forcite module, leveraging the COMPASS II force field for potential energy assessments. These simulations were performed under the NVT ensemble at 298 K, with temperature governed by the Nose–Hoover technique. The energy and force convergence thresholds were established at 1.0×10^4 kcal mol^{-1} and 0.005 kcal mol^{-1} $Å^{-1}$, respectively. A time increment of 1 fs was utilized throughout the simulations.

3 Results and Discussion

3.1 Adsorption Behavior and Interfacial Regulation of SCL on Zinc Surface

Figure 1a compares the adsorption energies. Owing to the rich hydroxyl groups (Fig. S1), the SCL/Zn(002) facet shows a lower adsorption energy than the water/Zn(002) facet, suggesting that SCL has a thermodynamic tendency

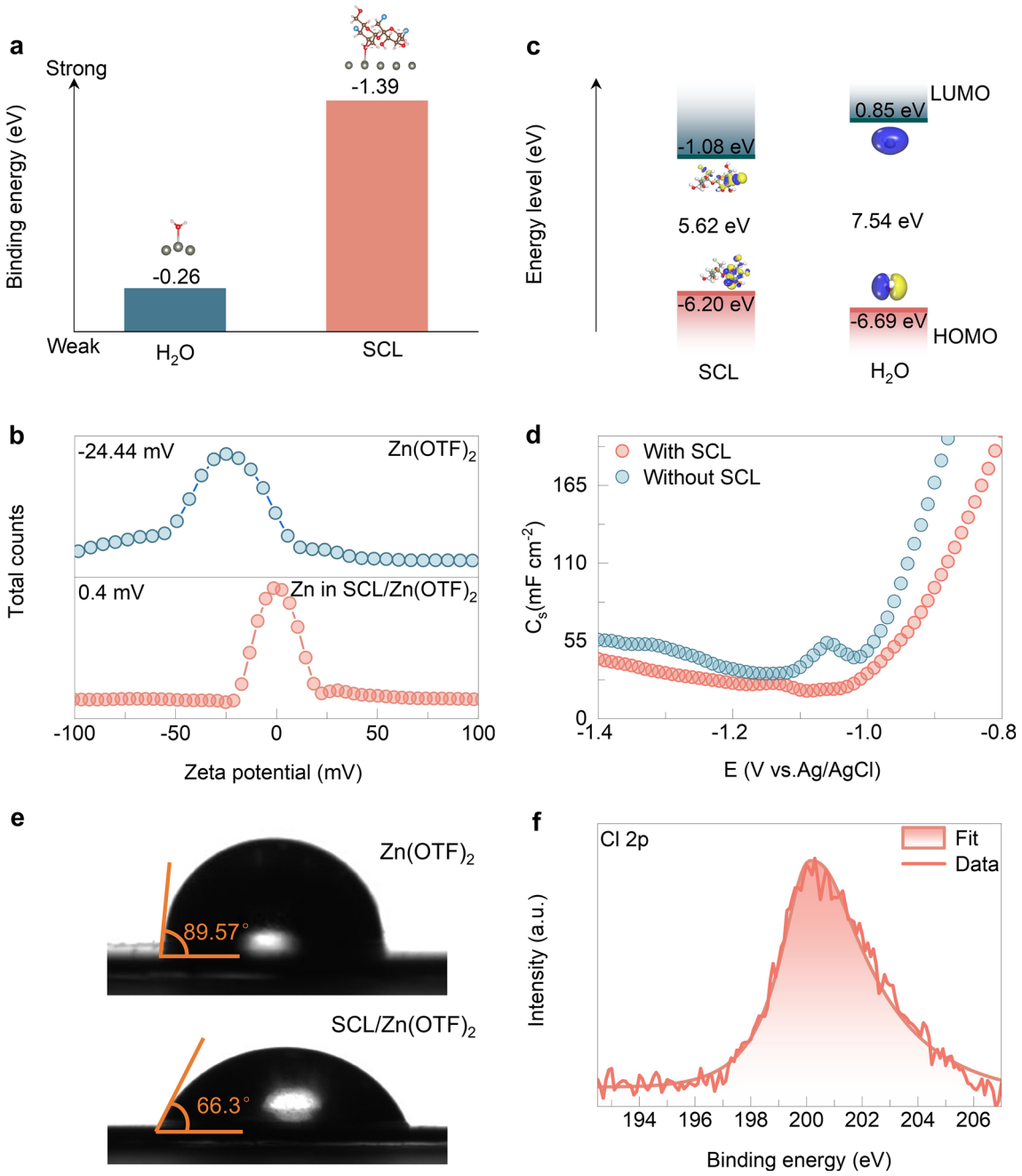

Fig. 1 **a** Adsorption energy of H_2O and SCL molecules on the Zn (002) surface. **b** Zeta potential of zinc powder with and without SCL additive. **c** HOMO and LUMO energy levels of SCL and H_2O. **d** Differential capacitance curve for Zn in Na_2SO_4 solution with/without SCL additive. **e** Contact angles between $Zn(OTF)_2$ and Zn foil, $SCL/Zn(OTF)_2$ and Zn foil. **f** The Cl 2*p* XPS spectra of Zn in $SCL/Zn(OTF)_2$ solution

for adsorption onto Zn surfaces. The presence of SCL in the electric double layer (EDL) significantly modifies the charge distribution on the surface of the Zn electrode, leading to reduced aggregation of H_2O molecules, which can effectively mitigate zinc corrosion and suppress side reactions. In this work, the optimal concentration of SCL is determined to be 5 wt% which is comprehensively discussed and illustrated in Fig. S2. As shown in Fig. 1b, the addition of SCL leads to a substantial increase of zeta potential from -24.44 to 0.4 mV, indicating a significant enhancement in

 https://doi.org/10.1007/s40820-025-01954-3

surface charge modulation. Figure S3 shows the 3D differential charge density; the SCL reveals a significant overlap of electron clouds and charge transfer with the Zn surface, indicating the strong interaction between SCL and Zn [22, 23].

Figure 1c shows the energy levels of molecular orbitals. Compared with the H_2O (− 6.69 eV), the higher HOMO energy level of SCL (-6.2 eV) suggests that SCL is more likely to lose electrons and adsorb onto the zinc surface [24], regulating the interfacial structure, as confirmed by the reduced capacity in Fig. 1d [25]. The electrostatic potential mapping in Fig. S4 further proves that the rich hydroxyl groups of the SCL molecule can offer multiple binding sites for H_2O and cations [26]. Consequently, the SCL/$Zn(OTF)_2$ electrolyte shows better zincophilic features than the $Zn(OTF)_2$ electrolyte (Fig. 1e) [27]. After immersing zinc foil in the SCL/$Zn(OTF)_2$ electrolyte for a certain time, the XPS data displays characteristic Cl 2*p* peaks at 200 eV corresponding to organo-chlorine species (Fig. 1f) [28], and no peak is observed when using pure $Zn(OTF)_2$ (Fig. S5). All the above findings demonstrate that SCL can effectively adsorb onto the zinc surface and regulate the surface structure. As illustrated in Fig. S6, introducing SCL into the $Zn(OTF)_2$ electrolyte facilitates the approach of SCL molecules to the inner Helmholtz plane (IHP) of the electric double layer (EDL) at the zinc surface. Owing to the favorable zincophilic characteristics, the SCL molecules will replace some active sites previously occupied by water molecules and the modified Zn/electrolyte interface can suppress side reactions and regulate Zn deposition behavior [29].

3.2 Effect of SCL on Electrolyte Properties

Figure 2a exhibits the linear sweep voltammetry (LSV) data. Compared with the $Zn(OTF)_2$ electrolyte, the SCL/$Zn(OTF)_2$ electrolyte shows an onset potential shift from 0.26 to − 0.14 V, indicating the suppression of HER. The increased overpotential for OER further endorses the beneficial impact of the SCL additive in mitigating water decomposition [30]. The Gibbs free energies (ΔG) are employed to quantify the thermodynamic energy barrier associated with the HER occurring on the Zn anode (Fig. S7). The Zn anode in the SCL/$Zn(OTF)_2$ electrolyte exhibits a higher energy barrier (ΔG = 1.078 eV) compared to that in the $Zn(OTF)_2$ electrolyte (ΔG = 0.992 eV), suggesting that the SCL/$Zn(OTF)_2$ electrolyte possesses a greater capability to suppress HER. After adding the SCL, the pH value increases from 5.06 to 5.56, which can enhance the corrosion resistance of the SCL/$Zn(OTF)_2$ electrolyte (Fig. S8). As evidenced by the Tafel test results (Fig. S9), the SCL/$Zn(OTF)_2$ electrolyte demonstrates a lower corrosion current density and a higher corrosion potential than the $Zn(OTF)_2$ electrolyte [31]. Additionally, the surface morphology observations of zinc electrodes after being immersed in the SCL/$Zn(OTF)_2$ electrolyte provide further evidence of the corrosion mitigation effect of the SCL/$Zn(OTF)_2$ electrolyte (Fig. S10). Compared to $Zn(OTF)_2$, no distinct characteristic peaks associated with the by-product, *e.g.,* $Zn_x(OTF)_y(OH)_{2x-y}{\cdot}nH_2O$ [32, 33], were observed on the Zn plate immersed in the SCL/$Zn(OTF)_2$ electrolyte (Fig. S11). To further evaluate the interfacial stability, Zn//Zn symmetric batteries were tested galvanostatically (Fig. S12). In the SCL/$Zn(OTF)_2$ electrolyte, the Zn anode's interfacial impedance decreased progressively with cycling and stabilized by the 10th cycle. By contrast, in the $Zn(OTF)_2$ electrolyte, impedance dropped sharply after the first cycle, then fluctuated erratically. This discrepancy likely stems from by-product accumulation and interfacial degradation due to irregular Zn deposition.

Molecular dynamics (MD) simulations were conducted to investigate the solvation structures of Zn^{2+} in the hybrid electrolyte. Figure 2b demonstrates that SCL effectively displaces H_2O molecules within the primary solvation shell, thereby reconstructing the solvation structure of Zn^{2+}. The activation energy (Ea) for the Zn interface in the SCL/$Zn(OTF)_2$ electrolyte was calculated to be 27.0 kJ mol^{-1} (Fig. S13), markedly lower than the 34.8 kJ mol^{-1} observed in the $Zn(OTF)_2$ electrolyte. This reduction in the de-solvation energy barrier suggests that the incorporation of SCL into the Zn^{2+} solvation sheath can significantly accelerate de-solvation kinetics by modulating the local environment around Zn^{2+}. The influence of SCL on the $Zn(OTF)_2$ electrolyte environment was confirmed by FTIR (Fig. 2c). The blue shift in both the O–H stretching vibration (3000–3700 cm^{-1}) [34, 35] and the O–H bending vibration (1500–1700 cm^{-1}) [36, 37] indicates reduced hydrogen bond interaction among H_2O molecules, which will lead to a weakened water activity. Figure 2d presents the ^1H nuclear magnetic resonance (NMR) spectra. With the addition of SCL, the ^1H signal of H_2O shifts to a lower field, suggesting the reduced electron density at the ^1H position, which is induced by the disruption of the original hydrogen-bonding network. As shown in

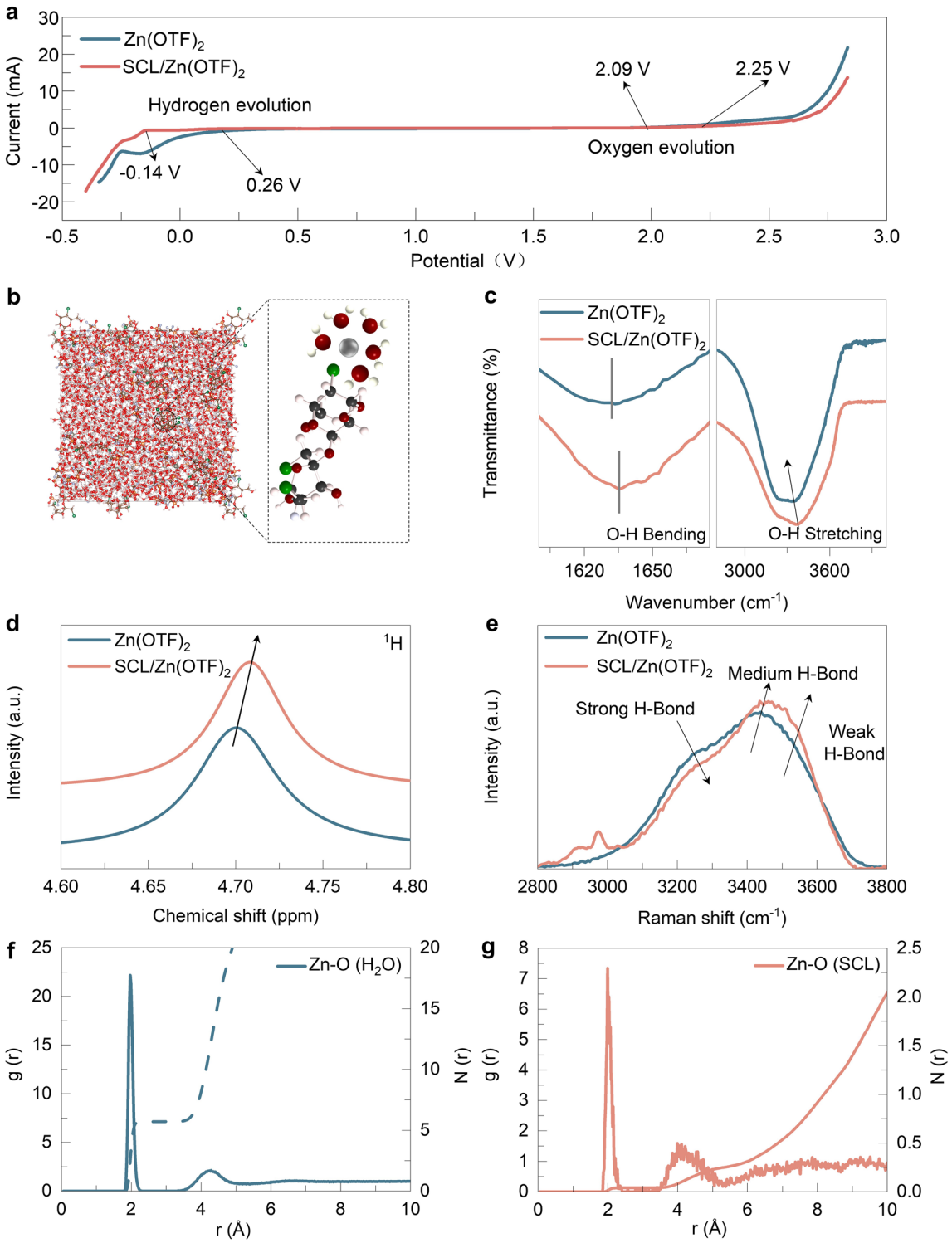

Fig. 2 **a** LSV curves in $Zn(OTF)_2$ and $SCL/Zn(OTF)_2$ electrolytes. **b** Snapshots of the MD simulation of $SCL/Zn(OTF)_2$ electrolyte. **c** FTIR spectra of $Zn(OTF)_2$ and $SCL/Zn(OTF)_2$ electrolytes. **d** ^1H NMR spectra of different electrolytes. **e** Raman spectrum of different electrolytes. RDFs of **f** Zn–O (H_2O), **g** Zn–O (SCL) collected from MD simulations in $SCL/Zn(OTF)_2$ electrolyte

https://doi.org/10.1007/s40820-025-01954-3

Fig. 2e, after the introduction of SCL, the strong hydrogen bond peak narrows markedly, while the medium and weak hydrogen bond peaks broaden, which indicates that free water with hydrogen bonds is significantly broken, reducing water activity.

The effects of SCL on the $Zn(OTF)_2$ electrolyte environment were further validated through radial distribution functions (RDFs) and coordination numbers (N(r)). As illustrated in Fig. 2d, e, the primary peaks corresponding to the Zn–O pair from both SCL and H_2O are observed at ~ 2 Å within the SCL/$Zn(OTF)_2$ system. The coordination numbers for Zn–O (H_2O) and Zn–O (SCL) are determined to be 5.71 and 0.04, respectively. This finding indicates that SCL successfully participates in the first solvation shell of Zn^{2+} ions [38]. The ab initio molecular dynamics (AIMD) simulation reveals the stable adsorption of SCL on the Zn surface, which can effectively inhibit water molecules from interacting with the Zn surface (Fig. S14).

3.3 Influence of SCL on Zinc Deposition Behavior

The actual plating process of Zn^{2+} was directly observed using in situ optical microscopy. In the $Zn(OTF)_2$ electrolyte, ongoing the plating, prominent Zn dendrites appeared on the surface of the Zn electrode (Fig. 3a). In contrast, no dendrites were detected on the surface of the Zn electrode even after 30 min of plating in the SCL/$Zn(OTF)_2$ electrolyte. To more accurately assess the influence of the SCL additive on the deposition behavior of Zn^{2+}, the zinc layers deposited in different electrolytes were analyzed using XRD. The relative texture coefficient (RTC) of Zn deposition in the SCL/$Zn(OTF)_2$ and $Zn(OTF)_2$ electrolytes with the current density of 30 mA cm^{-2} is calculated using the following equation [39, 40]:

$$\mathrm{RCT}_{(\mathrm{HKL})} = \frac{I_{(\mathrm{HKL})}/I_{0(\mathrm{HKL})}}{\Sigma\left[I_{(\mathrm{HKL})}/I_{0(\mathrm{HKL})}\right]} \times 100\% \quad (3)$$

The RTC value can be used to assess zinc deposition orientation and crystal growth behavior during electroplating. As the RTC value increases, electroplated Zn tends to align horizontally. On the contrary, as the RTC values decreases, the deposited Zn tends to be irregularly inclined Zn dendrites. As shown in Fig. 3b, Zn deposited with SCL shows a continuous increase in the peak intensity of Zn (002) crystal facet during the plating process, the RTC value increased from 20 to 47 and 76 after 20, 40 and 60 min of deposition (Fig. S15), respectively. When deposition in $Zn(OTF)_2$ electrolyte with the same condition, the RTC value exhibited minimal variation during the electroplating process. At other current densities, the addition of SCL shows the same influence on the Zn depositing behavior (Fig. S16). The preferential (002) texture favors the uniform and consistent growth of Zn. As shown by the SEM observation (Fig. 3c, d), the Zn anode deposited in the $Zn(OTF)_2$ electrolyte exhibits nonuniform deposition at 20 mA cm^{-2}—20 mAh cm^{-2}. In the SCL/$Zn(OTF)_2$ electrolyte, the deposited Zn shows a clear hexagonal shape and is closely packed, consistent with the optical observation. As the current density increases, the deposited zinc shows a more uniform and compact surface (Fig. S17). To further investigate the stability of the influence exerted by SCL during cycling, we conducted SEM characterization to examine the morphology of Zn anodes. After 10 cycles, the Zn in the blank group displays uneven growth accompanied by the gradual emergence of dendrites. In contrast, the Zn in the SCL/$Zn(OTF)_2$ group exhibits uniform growth characterized by numerous horizontally aligned Zn plates on its surface (Figs. S18 and S19).

Figure 3e presents the side views of Zn atom adsorption configurations on the (100), (101), and (002) crystallographic planes, along with the adsorption energies, respectively. After adsorbing SCL onto three different Zn facets, the adsorption energy of Zn atoms on Zn (002)-SCL shows the lowest value (absolute value). According to Bravais' law, the orientation of crystal planes is determined by the ion deposition rates on various planes. The plane with the slowest growth rate tends to become the dominant exposed facet [41]. When Zn(002), (100), and (101) coexist, newly electroplated zinc tends to nucleate and grow preferentially on the (100) and (101) facets due to their higher adsorption energy. The selective growth leads to the formation of a flat, preferred (002) texture.

The Zn^{2+} deposition rate discrepancies across diverse crystal planes are further interpreted via Zn^{2+} migration energy. On the SCL-adsorbed Zn crystal surface, the migration energy of Zn^{2+} ions at different sites is lower on the Zn(002) plane compared to the Zn(100) and (101) planes (Figs. 4a and S20), which implies a more rapid migration of Zn ions on the Zn(002) plane Consequently, Zn ions can easily diffuse along the Zn(100) and (101) directions to other planes, facilitating the exposure of the layered Zn(002)

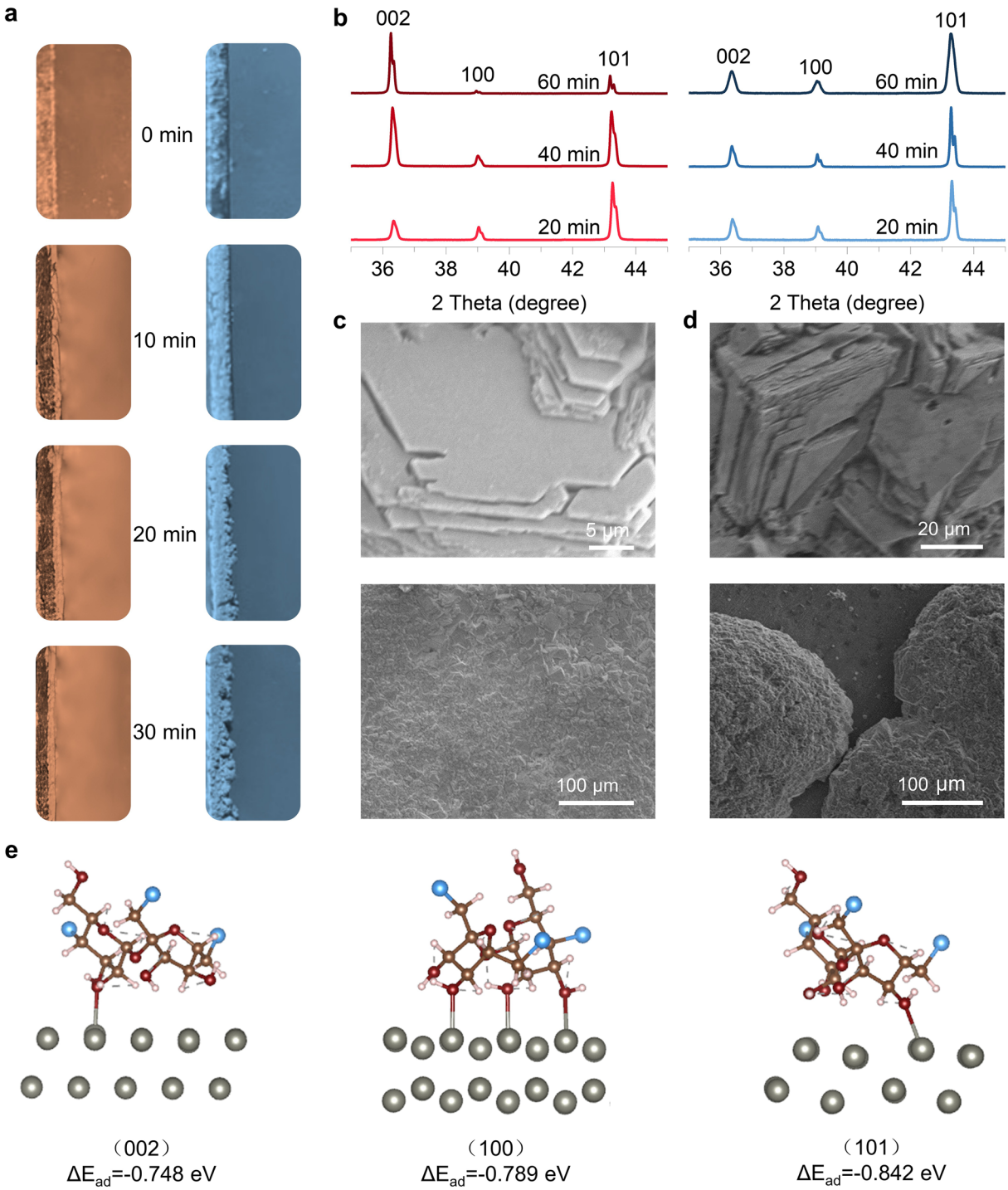

Fig. 3 **a** In situ optical microscopic observations of Zn deposition in the SCL/$Zn(OTF)_2$ (the left) and $Zn(OTF)_2$ (the right) electrolytes with the current density of 30 mA cm^{-2}. **b** XRD patterns of the fabricated Zn layer in SCL/$Zn(OTF)_2$ (the left) and $Zn(OTF)_2$ (the right) electrolyte systems with varying deposition times under 30 mA cm^{-2}. SEM image of Zn deposits at 30 mA cm^{-2} in **c** SCL/$Zn(OTF)_2$ and **d** $Zn(OTF)_2$ electrolyte. **e** Zn ion adsorption energy on different crystal planes after SCL is adsorbed on the Zn slab

https://doi.org/10.1007/s40820-025-01954-3

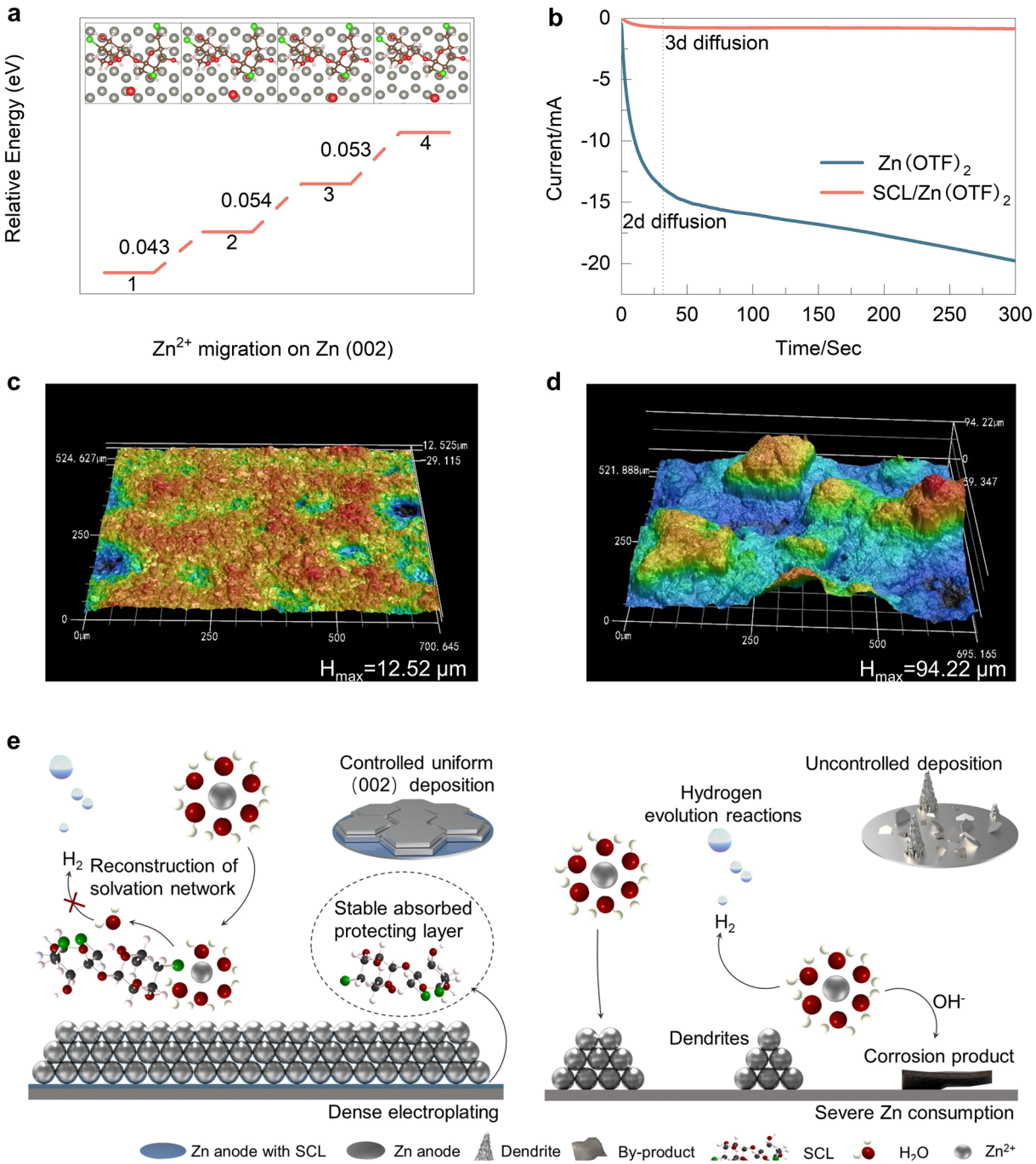

Fig. 4 **a** Zn^{2+}migration energy on Zn (100) after SCL adsorption, insets show the calculated migration positions. **b** CA profiles in different electrolytes under a fixed overpotential of − 150 mV. The 3D surface topographies of the deposited Zn electrodes surface in **c** SCL/$Zn(OTF)_2$ electrolyte and **d** $Zn(OTF)_2$ electrolyte at 30 mA cm^{-2}. **e** Schematic illustration of Zn plating behavior with and without SCL additive

texture. This phenomenon can be deemed as homoepitaxial growth [42]. The nucleation and deposition behavior of the Zn electrode were investigated using the chronoamperometry (CA) technique by analyzing the current responses at a fixed overpotential of − 150 mV (Fig. 4b). The deposition in $Zn(OTF)_2$ electrolyte exhibits a continuously increasing current over 300 s, suggesting uncontrolled 2D diffusion of Zn^{2+} ions [43, 44]. This phenomenon can be attributed to the continuous increase in electrode surface area caused by the formation of the "tip effect" [45]. The elevated nucleation

overpotential observed in the CV curves (Fig. S21) indicates that the SCL additive enhances the initial nucleation barrier of the Zn anode by promoting its adsorption, leading to the formation of finer nuclei and a decelerated nucleation process within the SCL/$Zn(OTF)_2$ system, which in turn enables the development of a dense deposition layer. In systems that incorporate SCL, the trend of increasing current is relatively moderate, demonstrating that the SCL can suppress Zn dendrite growth. The 3D confocal laser scanning microscopy (CLSM) images in Fig. 4c, d visually show the surface state of the deposited Zn. The addition of SCL leads to a smooth surface. While in the $Zn(OTF)_2$ electrolyte, the deposited Zn exhibits significant inhomogeneity and features numerous sharp protrusions.

Based on the experimental results and computational analyses, it can be concluded that the introduction of SCL can effectively direct the uniform plating of Zn^{2+}. As illustrated by Fig. 4e, the SCL additive can not only disrupt the solvation structure around zinc ions and reduce water activity but also preferentially adsorb onto the Zn(002) crystal surface, inducing stable zinc deposition and slowing down both nucleation and diffusion of Zn^{2+}, promoting enhanced exposure of the Zn(002) crystal facet. Meanwhile, SCL adsorbed on the zinc anode surface serves to prevent direct contact between free water and zinc foil, acting as a protective barrier that further inhibits HER and corrosion.

3.4 Electrochemical Performance of Batteries with SCL Additive

The electrochemical performance of Zn//Zn and Zn//Cu batteries with and without SCL was tested. At 1 mA cm^{-2}–1 mAh cm^{-2} (Figs. 5a and S22), the battery with SCL/$Zn(OTF)_2$ shows much longer cycling time (4900 h) compared with that in $Zn(OTF)_2$ (224 h). Even at a higher current density and areal capacity of 30 mA cm^{-2} and 30 mAh cm^{-2} (DOD = 73.3%), the battery still exhibits stable cycling performance for 171 h, accompanied by steady potential profiles (Fig. 5b). Practical applications require the evaluation of Zn electrodes' endurance capabilities under the concurrent challenges of high current densities, high areal capacities, and deep depths of discharge. With a much higher DOD of 97.7% (30 mA cm^{-2}–40 mAh cm^{-2}), a lifespan of 98 h can still be achieved for the Zn//Zn batteries (Fig. 5c), which is superior to many previously reported works (Table S1). Figure S23 shows the digital photos of Zn//Zn symmetric battery after cycling. Clearly, the battery with the SCL/$Zn(OTF)_2$ electrolyte shows reduced volume expansion than that with $Zn(OTF)_2$, indicating a suppressed HER [46]. The rate performance (Fig. S24) further demonstrates that the batteries can stably operate using the SCL/$Zn(OTF)_2$ electrolyte across a broad current density range, from 1 to 30 mA cm^{-2}. Figure. S25 shows the coulombic efficiency of Zn//Cu battery at 0.5 mA cm^{-2} and 0.5 mAh cm^{-2}. With the SCL/$Zn(OTF)_2$ electrolyte, the Zn//Cu battery exhibits excellent reversibility for 1000 cycles and the average CE is as high as 99.84%. Currently, reported CE values are typically obtained at current densities of 0.5 mA cm^{-2} or higher, as elevated current densities tend to obscure the effects of the HER, which will lead to a high CE value [47]. Here, to show the superiority of the SCL/$Zn(OTF)_2$ electrolyte, at a very low current density of 0.2 mA cm^{-2} and low area capacity of 0.2 mAh cm^{-2}, we tested the coulombic efficiency of Zn//Cu batteries. As shown in Figs. 4d and S26, the Zn//Cu battery with the SCL/$Zn(OTF)_2$ electrolyte still shows a high CE of 99.61% and maintains a long lifespan of over 4000 h, superior to that with $Zn(OTF)_2$ electrolyte and previously reported works (Table S2), indicating the high reversibility of Zn plating/stripping induced by the addition of SCL.

Next, Zn//$NH_4V_4O_{10}$ full batteries were assembled to investigate the feasibility of SCL/$Zn(OTF)_2$ electrolyte in practical battery systems. The CV profiles of the Zn//$NH_4V_4O_{10}$ batteries employing the SCL/$Zn(OTF)_2$ and $Zn(OTF)_2$ electrolytes indicate that the incorporation of SCL has negligible influence on the redox behavior of the $NH_4V_4O_{10}$ cathode (Fig. S27). However, as shown in Fig. 5e, at 500 mA g^{-1}, the battery with SCL/$Zn(OTF)_2$ electrolyte demonstrates a long lifespan, achieving a capacity retention of 90.7% (420 mAh g^{-1} after 500 cycles). In contrast, the battery without SCL becomes inoperative after only 203 cycles. Figure. S28 presents the corresponding voltage profiles at specific cycle numbers under a current density of 500 mA g^{-1}, illustrating enhanced capacity retention with SCL/$Zn(OTF)_2$ electrolyte. Furthermore, the cycling performance of full battery at 5 A g^{-1} shows 84.9% capacity retention after 4000 cycles (Figs. S29 and S30). Figure. S31 presents the rate performance of Zn//$NH_4V_4O_{10}$ full batteries, indicating that the battery incorporating SCL exhibits superior rate performance. To further validate its potential application, we fabricated a Zn//$NH_4V_4O_{10}$ pouch cell utilizing an

 https://doi.org/10.1007/s40820-025-01954-3

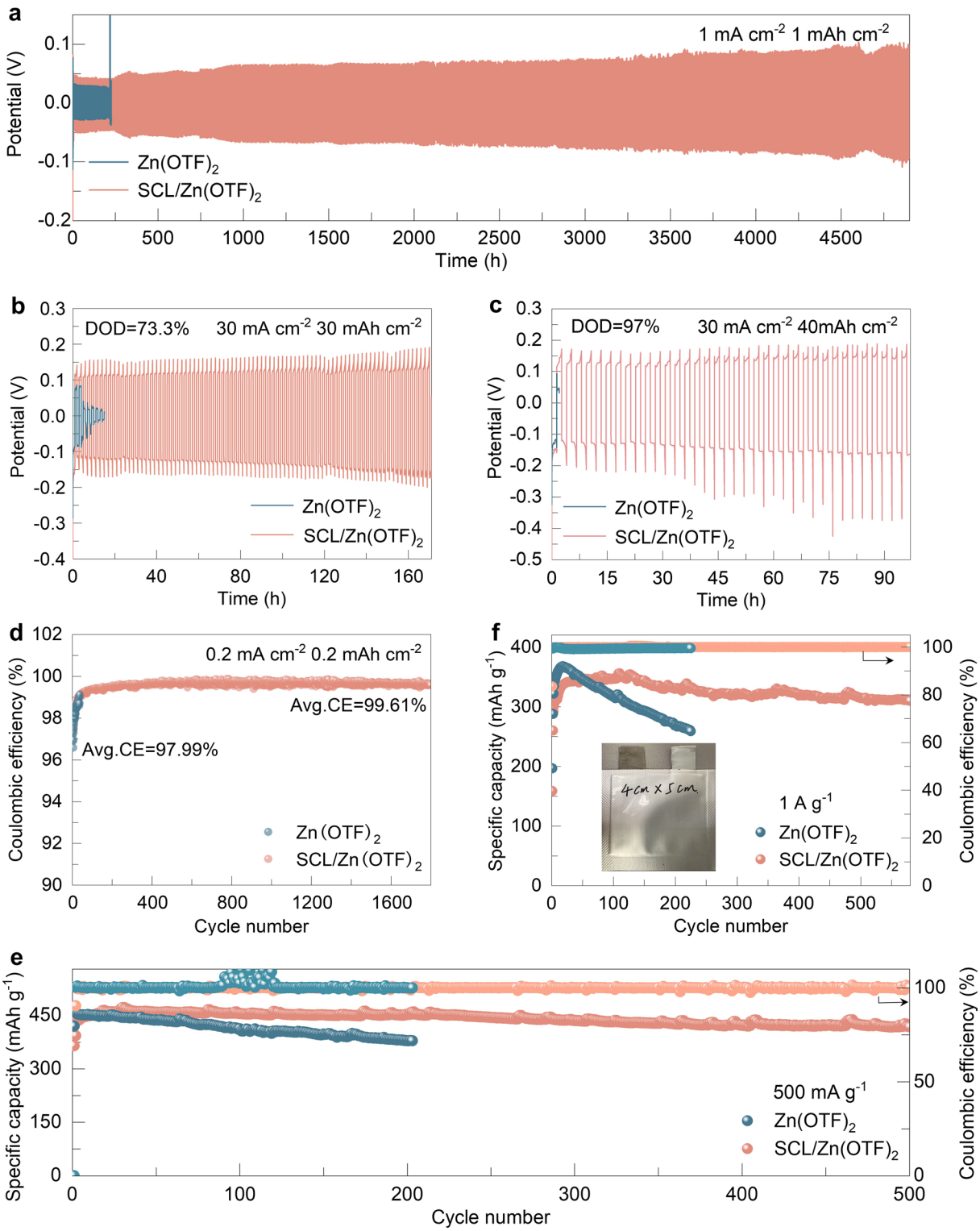

Fig. 5 **a** Galvanostatic cycling of Zn//Zn battery in bare $Zn(OTF)_2$ and SCL/$Zn(OTF)_2$ electrolyte at 1 mA cm^{-2}, 1 mAh cm^{-2}. **b** Galvanostatic cycling of Zn//Zn battery with a limited Zn supply (DOD_{Zn} = 73.3%) in SCL/$Zn(OTF)_2$ electrolyte at 30 mA cm^{-2}, 30 mAh cm^{-2}. **c** Galvanostatic cycling of Zn//Zn battery with a limited Zn supply (DOD_{Zn} = 97%) in SCL/$Zn(OTF)_2$ electrolyte at 30 mA cm^{-2}, 40 mAh cm^{-2}. **d** CE of Zn//Cu half batteries with various electrolytes at 0.2 mA cm^{-2}, 0.2 mAh cm^{-2}. **e** Long-term cycling performance and corresponding CEs of Zn//$NH_4V_4O_{10}$ full batteries at 500 mA g^{-1}. **f** Electrochemical performance of $NH_4V_4O_{10}$//Zn pouch cells operated in bare $Zn(OTF)_2$ and SCL/$Zn(OTF)_2$ electrolyte at 1 A g^{-1} (mass loading = 1.5 mg cm^{-2}, N/P = 39.2, E/C = 33.5 μL $mAh.^{-1}$)

electrolyte augmented with SCL for cyclic evaluation. The pouch cell was assembled with single anode and cathode components within dimensions of 20 cm^2 (4 cm × 5 cm). With SCL/$Zn(OTF)_2$ electrolyte, the pouch cell maintains a reversible capacity of 311 mAh g^{-1} over 580 cycles at a current density of 1 A g^{-1} (Fig. 5f), superior to that using the $Zn(OTF)_2$ electrolyte.

4 Conclusion

In conclusion, an electrolyte engineering strategy was proposed to address critical issues related to dendrite growth and by-product generation, aiming to enhance the long-term stability of zinc-ion batteries. After introducing sucralose (SCL) into the electrolyte, the as-formed SCL adsorption layer on the Zn surface leads to the exposure of (002) facet which promotes horizontal deposition of Zn and can effectively restrict side reactions. Employing the SCL/$Zn(OTF)_2$ electrolyte, the Zn//Zn symmetric battery can stably run for 4900 h at 1 mA cm^{-2}–1 mAh cm^{-2} and 171 h at 30 mA cm^{-2}–30 mAh cm^{-2} (depth of discharge, DOD = 73.3%). Even at an ultrahigh DOD of 97.7% (30 mA cm^{-2}–40 mAh cm^{-2}), the Zn//Zn symmetric battery can maintain for 98 h. At a very low current density of 0.2 mA cm^{-2} and small area capacity of 0.2 mAh cm^{-2}, the Zn//Cu half battery shows a high average CE of 99.61% and a long lifespan over 4000 h, indicating high reveribility and stability of the Zn anode enabled by the SCL. With the SCL/$Zn(OTF)_2$ electrolyte, the Zn//$NH_4V_4O_{10}$ full battery delivers 420 mAh g^{-1} at 500 mA g^{-1} after 500 cycles, retaining 90.7% of its capacity. Additionally, the pouch cell maintains a reversible capacity of 311 mAh g^{-1} over 580 cycles when operated at 1 A g^{-1}. This work provides a practical and efficient electrolyte additive to drive the practical development of AZIBs.

Acknowledgements This work was supported by the Anhui Provincial Science and Technology Innovation Initiative (202423i08050051), the Anhui Provincial Natural Science Foundation (2408085MB029), the HFIPS Director's Fund (YZJJGZX202201), and the Natural Science Foundation of Hebei Province of China (B2024402018). A portion of this work was performed at the Steady High Magnetic Field Facilities, High Magnetic Field Laboratory, Chinese Academy of Sciences. The numerical computation was performed on Hefei advanced computing center.

Author Contributions Feiyu Tao was involved in experiments, data curation, conceptualization, and original draft writing. Yingke Ren, Li'e Mo, Yifan Wang, Yang Huang, Hong Zhang, and Chengwu Shi were involved in experiments. Jiaqin Liu, Lei Chen, Linhua Hu, and Yucheng Wu were involved in experiments, original draft writing, and review. Zhaoqian Li was involved in guidance, review, supervision, and funding acquisition.

Declarations

Conflict of Interest The authors declare no interest conflict. They have no known competing financial interests or personal relationships that could have appeared to influence the work reported in this paper.

Supplementary Information The online version contains supplementary material available at https://doi.org/10.1007/s40820-025-01954-3.

References

1. X. Yi, H. Fu, A.M. Rao, Y. Zhang, J. Zhou et al., Safe electrolyte for long-cycling alkali-ion batteries. Nat. Sustain. **7**(3), 326–337 (2024). https://doi.org/10.1038/s41893-024-01275-0
2. Z. Hu, J. Hao, D. Shen, C. Gao, Z. Liu et al., Electro-spraying/spinning: a novel battery manufacturing technology. Green Energy Environ. **9**(1), 81–88 (2024). https://doi.org/10.1016/j.gee.2022.05.004
3. Z. Li, Y. Ren, L. Mo, C. Liu, K. Hsu et al., Impacts of oxygen vacancies on zinc ion intercalation in VO_2. ACS Nano **14**(5), 5581–5589 (2020). https://doi.org/10.1021/acsnano.9b09963
4. Z. Wu, F. Ye, Q. Liu, R. Pang, Y. Liu et al., Simultaneous incorporation of V and Mn element into polyanionic NASICON for high energy-density and long-lifespan Zn-ion storage. Adv. Energy Mater. **12**(23), 2200654 (2022). https://doi.org/10.1002/aenm.202200654
5. H. Niu, H. Liu, L. Yang, T. Kang, T. Shen et al., Impacts of distorted local chemical coordination on electrochemical performance in hydrated vanadium pentoxide. Nat. Commun. **15**(1), 9421 (2024). https://doi.org/10.1038/s41467-024-53785-2

6. Q. Zong, Y. Zhuang, C. Liu, Q. Kang, Y. Wu et al., Dual effects of metal and organic ions co-intercalation boosting the kinetics and stability of hydrated vanadate cathodes for aqueous zinc-ion batteries. Adv. Energy Mater. **13**(31), 2301480 (2023). https://doi.org/10.1002/aenm.202301480
7. H. Tian, G. Feng, Q. Wang, Z. Li, W. Zhang et al., Three-dimensional Zn-based alloys for dendrite-free aqueous Zn battery in dual-cation electrolytes. Nat. Commun. **13**(1), 7922 (2022). https://doi.org/10.1038/s41467-022-35618-2
8. Y. Zhu, H. Li, X. Sun, A. Chen, R. Hou et al., Minimizing Zn loss through dual regulation for reversible zinc anode beyond 90% utilization ratio. Small **21**(10), 2411986 (2025). https://doi.org/10.1002/smll.202411986
9. K. Guan, W. Chen, Y. Yang, F. Ye, Y. Hong et al., A dual salt/dual solvent electrolyte enables ultrahigh utilization of zinc metal anode for aqueous batteries. Adv. Mater. **36**(38), 2405889 (2024). https://doi.org/10.1002/adma.202405889
10. Y. Gao, N. Yang, F. Bu, Q. Cao, J. Pu et al., Double-sided engineering for space-confined reversible Zn anodes. Energy Environ. Sci. **17**(5), 1894–1903 (2024). https://doi.org/10.1039/d3ee04292h
11. R. Wang, Y. Jia, Z. Kong, W. Wang, Y. Hu et al., Stabilization strategies for zinc anode interfaces under high discharge depth. J. Energy Storage **105**, 114642 (2025). https://doi.org/10.1016/j.est.2024.114642
12. S. Chen, K. Ouyang, Y. Liu, M. Cui, G. Pu et al., Non-epitaxial electrodeposition of overall 99 % (002) plane achieves extreme and direct utilization of 95% Zn anode and by-product as cathode. Angew. Chem. Int. Ed. **63**(42), e202409303 (2024). https://doi.org/10.1002/anie.202409303
13. S.D. Pu, B. Hu, Z. Li, Y. Yuan, C. Gong et al., Decoupling, quantifying, and restoring aging-induced Zn-anode losses in rechargeable aqueous zinc batteries. Joule **7**(2), 366–379 (2023). https://doi.org/10.1016/j.joule.2023.01.010
14. Z. Huang, Z. Li, Y. Wang, J. Cong, X. Wu et al., Regulating Zn(002) deposition toward long cycle life for Zn metal batteries. ACS Energy Lett. **8**(1), 372–380 (2023). https://doi.org/10.1021/acsenergylett.2c02359
15. X. Li, Z. Chen, P. Ruan, X. Hu, B. Lu et al., Inducing preferential growth of the Zn (002) plane by using a multifunctional *chelator* for achieving highly reversible Zn anodes. Nanoscale **16**(6), 2923–2930 (2024). https://doi.org/10.1039/d3nr05699f
16. W. Xie, K. Zhu, W. Jiang, H. Yang, M. Ma et al., Highly 002-oriented dendrite-free anode achieved by enhanced interfacial electrostatic adsorption for aqueous zinc-ion batteries. ACS Nano **18**(32), 21184–21197 (2024). https://doi.org/10.1021/acsnano.4c04181
17. X. Chen, Z. Zhai, T. Yu, X. Liang, R. Huang et al., Constructing a 3D zinc anode exposing the Zn(002) plane for ultralong life zinc-ion batteries. Small **20**(35), 2401386 (2024). https://doi.org/10.1002/smll.202401386
18. Q. Zong, B. Lv, Y. Yu, Q. Zhang, S. Zhou et al., Close-packed growth and buffer action enabling stable and reversible Zn anode. Nano Energy **136**, 110725 (2025). https://doi.org/10.1016/j.nanoen.2025.110725
19. Y. Li, X. Ma, X. Zhang, F. Zhang, Q. Wang et al., High Zn(002)-preferential orientation enabled by a proton additive for dendrite-free zinc anodes. Energy Environ. Sci. **17**(23), 9205–9214 (2024). https://doi.org/10.1039/D4EE03276D
20. X. Song, L. Bai, C. Wang, D. Wang, K. Xu et al., Synergistic cooperation of Zn(002) texture and amorphous zinc phosphate for dendrite-free Zn anodes. ACS Nano **17**(15), 15113–15124 (2023). https://doi.org/10.1021/acsnano.3c04343
21. W. Yuan, X. Nie, G. Ma, M. Liu, Y. Wang et al., Realizing textured zinc metal anodes through regulating electrodeposition current for aqueous zinc batteries. Angew. Chem. Int. Ed. **62**(10), e202218386 (2023). https://doi.org/10.1002/anie.202218386
22. T.C. Li, C. Lin, M. Luo, P. Wang, D.-S. Li et al., Interfacial molecule engineering for reversible Zn electrochemistry. ACS Energy Lett. **8**(8), 3258–3268 (2023). https://doi.org/10.1021/acsenergylett.3c00859
23. Y. Xiong, W. Teng, Z. Zhao, S. Xu, Y. Ma et al., Effective control of the solution environment in aqueous Zinc-ion batteries for promoting (002)-textured zinc growth by a bio-electrolyte additive. Energy Storage Mater. **74**, 103959 (2025). https://doi.org/10.1016/j.ensm.2024.103959
24. T. Xue, Y. Mu, Z. Zhang, J. Guan, J. Qiu et al., Enhanced zinc deposition and dendrite suppression in aqueous zinc-ion batteries *via* citric acid-aspartame electrolyte additives. Adv. Energy Mater. **15**(26), 2500674 (2025). https://doi.org/10.1002/aenm.202500674
25. Y. Ding, L. Yin, T. Du, Y. Wang, Z. He et al., A trifunctional electrolyte enables aqueous zinc ion batteries with long cycling performance. Adv. Funct. Mater. **34**(30), 2314388 (2024). https://doi.org/10.1002/adfm.202314388
26. T. Wei, Y. Peng, L. Mo, S. Chen, R. Ghadari et al., Modulated bonding interaction in propanediol electrolytes toward stable aqueous zinc-ion batteries. Sci. China Mater. **65**(5), 1156–1164 (2022). https://doi.org/10.1007/s40843-021-1841-5
27. C. Ji, Y. Luo, G. Guo, X. Li, C. Sun et al., Regulating the inner Helmholtz plane with an electrophilic cation additive enabled stacked stratiform growth for highly reversible Zn anodes. Energy Storage Mater. **71**, 103615 (2024). https://doi.org/10.1016/j.ensm.2024.103615
28. D. Luo, Z. Zhang, R. Sun, J. Ma, Z. Li et al., Environmentally friendly additives for crystal surface modulation and suppression of dendrites for aqueous zinc-ion batteries. J. Energy Storage **87**, 111375 (2024). https://doi.org/10.1016/j.est.2024.111375
29. X. Fan, L. Chen, Y. Wang, X. Xu, X. Jiao et al., Selection of negative charged acidic polar additives to regulate electric double layer for stable zinc ion battery. Nano Micro Lett. **16**(1), 270 (2024). https://doi.org/10.1007/s40820-024-01475-5
30. X. Zhu, Y. Wang, Y. Peng, H. Zhang, X. Zhang et al., Supramolecular interface buffer layer for stable zinc anode. Small Methods **9**(7), 2401865 (2025). https://doi.org/10.1002/smtd.202401865
31. C. Fan, W. Meng, J. Han, T. Li, D. Zuo et al., Self-regulating shielding layer induces (002) plane directional deposition of

zinc metal anode. Energy Storage Mater. **71**, 103554 (2024). https://doi.org/10.1016/j.ensm.2024.103554

32. P. Wang, Y. Zhong, J. Wang, H. Zhou, G. Sun et al., Boosting the anode and cathode stability simultaneously by interfacial engineering *via* electrolyte solvation structure regulation toward practical aqueous Zn-ion battery. Adv. Funct. Mater. **35**(5), 2414563 (2025). https://doi.org/10.1002/adfm.202414563
33. J. Chen, S. Bai, X. Zhang, J. Qiu, Z. Liu et al., Self-adsorbing electrolyte additive promoting Zn(002) deposition on Zn anode for aqueous zinc-ion battery. J. Colloid Interface Sci. **696**, 137870 (2025). https://doi.org/10.1016/j.jcis.2025.137870
34. F. Wu, J. Zhang, L. Ma, P. Ruan, Y. Chen et al., Directing Zn growth with biased adsorption of straight-chain molecules for superior Zn anode stability. Angew. Chem. Int. Ed. **64**(11), e202421787 (2025). https://doi.org/10.1002/anie.202421787
35. J. Wan, R. Wang, Z. Liu, L. Zhang, F. Liang et al., A double-functional additive containing nucleophilic groups for high-performance Zn-ion batteries. ACS Nano **17**(2), 1610–1621 (2023). https://doi.org/10.1021/acsnano.2c11357
36. Y. Wang, L.-E. Mo, X. Zhang, Y. Ren, T. Wei et al., Regulating water activity for all-climate aqueous zinc-ion batteries. Adv. Energy Mater. **14**(33), 2402041 (2024). https://doi.org/10.1002/aenm.202402041
37. Q. Zhao, W. Liu, X. Ni, H. Yu, C. Zhang et al., Steering interfacial renovation with highly electronegative Cl modulated trinity effect for exceptional durable zinc anode. Adv. Funct. Mater. **34**(41), 2404219 (2024). https://doi.org/10.1002/adfm.202404219
38. X. Chen, S. Li, K. Wang, H. Zhao, G. He et al., Halogenated solvation structure and preferred Zn (002) deposition *via* trace additive towards high reversibility for aqueous zinc-ion batteries. Energy Storage Mater. **73**, 103869 (2024). https://doi.org/10.1016/j.ensm.2024.103869
39. Y. Qin, H. Li, C. Han, F. Mo, X. Wang, Chemical welding of the electrode–electrolyte interface by Zn-metal-initiated *in situ* gelation for ultralong-life Zn-ion batteries. Adv. Mater. **34**(44), 2207118 (2022). https://doi.org/10.1002/adma.202207118
40. H. Zhang, Y. Zhong, J. Li, Y. Liao, J. Zeng et al., Inducing the preferential growth of Zn (002) plane for long cycle aqueous Zn-ion batteries. Adv. Energy Mater. **13**(1), 2203254 (2023). https://doi.org/10.1002/aenm.202203254
41. T. Wei, Y. Ren, Y. Wang, L.-E. Mo, Z. Li et al., Addition of dioxane in electrolyte promotes (002)-textured zinc growth and suppressed side reactions in zinc-ion batteries. ACS Nano **17**(4), 3765–3775 (2023). https://doi.org/10.1021/acsnano.2c11516
42. T. Wei, H. Zhang, Y. Ren, L.-E. Mo, Y. He et al., Building near-unity stacked (002) texture for high-stable zinc anode. Adv. Funct. Mater. **34**(14), 2312506 (2024). https://doi.org/10.1002/adfm.202312506
43. H. Wang, A. Zhou, X. Hu, Z. Song, B. Zhang et al., Facilitating oriented dense deposition: utilizing crystal plane end-capping reagent to construct dendrite-free and highly corrosion-resistant (100) crystal plane zinc anode. Adv. Mater. **36**(41), 2407145 (2024). https://doi.org/10.1002/adma.202407145
44. M. Liu, W. Yuan, X. Qu, X. Ru, X. Li et al., Superhydrophobic and robust hetero-metal-polymer hybrid interphase enables deep-cycling zinc metal anodes. Energy Environ. Sci. **17**(24), 9611–9622 (2024). https://doi.org/10.1039/d4ee04122d
45. T. Wei, Y. Ren, Z. Li, X. Zhang, D. Ji et al., Bonding interaction regulation in hydrogel electrolyte enable dendrite-free aqueous zinc-ion batteries from −20 to 60 °C. Chem. Eng. J. **434**, 134646 (2022). https://doi.org/10.1016/j.cej.2022.134646
46. Z. Jiang, Y. Wang, S. Zhai, C. Liu, A.Q. Zarifzoda et al., Guanidinium chloride as multifunctional electrolyte additives for highly reversible aqueous zinc batteries. Chem. Eng. J. **504**, 158924 (2025). https://doi.org/10.1016/j.cej.2024.158924
47. H. Jiang, L. Tang, Y. Fu, S. Wang, S.K. Sandstrom et al., Chloride electrolyte enabled practical zinc metal battery with a near-unity coulombic efficiency. Nat. Sustain. **6**(7), 806–815 (2023). https://doi.org/10.1038/s41893-023-01092-x

 https://doi.org/10.1007/s40820-025-01954-3